Journal of Computational Acoustics, Vol. 23, No. 4 (2015) 1540009 (14 pages)
© IMACS
DOI: 10.1142/S0218396X15400093

INTERNATIONAL ASSOCIATION
FOR MATHEMATICS AND
COMPUTERS IN SIMULATION

Pore Aspect Ratio Spectrum Inversion from Ultrasonic Measurements and Its Application

Fuyong Yan* and De-Hua Han†

Department of Earth and Atmospheric Sciences
University of Houston
Houston, Texas 77204, USA
**fyan@uh.edu*
†dhan@uh.edu

Xue-Lian Chen

School of Geosciences, China University of Petroleum
Qingdao 266580, P. R. China
chenxl@upc.edu.cn

Received 17 July 2015
Accepted 28 October 2015
Published 19 January 2016

We have conducted simultaneous ultrasonic velocity and pore volume change measurements on a carbonate rock sample. By including of pressure dependent porosity data, we have improved Cheng's pore aspect ratio spectrum inversion methodology and made the inverted pore aspect ratio spectrum more realistic. Tang's unified velocity dispersion and attenuation model is modified and extended to poroelastic media with complex pore structure under undrained condition. Using improved pore aspect ratio spectra inversion methodology and modified Tang's model, we have explored the potential application of pore aspect ratio spectrum in prediction of seismic wave dispersion and attenuation.

Keywords: Pore aspect ratio; ultrasonic; dispersion; attenuation.

1. Introduction

It is generally believed that the pressure dependency of rock seismic velocities is primarily caused by sequential closing of cracks or soft pores (Nur, 1969).[1–3] Although these cracks (also called soft pores) usually are volumetrically small, they can have significant saturation effects[2] on seismic velocities. The soft pores may also be important for dispersion and attenuation of seismic waves in porous rocks. During passing of the stress waves, the dispersion induced by interaction of the pore fluids between the soft pores and the stiff pores may be much stronger than that induced by the Biot flow, as shown in the ultrasonic measurement data by Han.[4] Several dual porosity (crack and stiff pore) models[5–9] are brought up to describe the dispersion and attenuation phenomena related to fluid interaction between soft crack pores and stiff pores. The double porosity model[10–12] can describe

dispersion and attenuation caused by heterogeneity of different scales. It is also possible to measure the velocity dispersion and attenuation of porous rock as function of frequency in laboratory,[13,14] but this technology is still in development and the measurement is much more expensive than regular ultrasonic velocity measurement.

In this study, we concentrate on study of the dispersion and attenuation induced by squirt flow and the Biot flow in complex pore system. The pore structure of the real rock is much more complicated than the dual porosity model.[15] One way to describe the complex pore system is using the pore aspect ratio spectrum. Based on Eshelby's[16] ellipsoidal inclusion theory and Kuster–Toksöz's model,[17] Cheng[3] uses the pressure dependent ultrasonic velocity data to invert the pore aspect ratio spectrum. The pore spectrum can also be derived from mercury injection data or NMR logging data. If we know the pore structure and the pore fluids, theoretically we should be able to predict the frequency dependent behavior of seismic velocities of porous rocks. This study aims to explore the feasibility to predict seismic wave dispersion and attenuation at a wide frequency range using the pore aspect ratio spectra inverted from the pressure dependent ultrasonic velocity and pore volume change measurement data.

2. Theory

Based on Eshelby's[16] study of elastic stress–strain field around an ellipsoidal inclusion, Cheng[3] derives the volume fractional change of the inclusion:

$$\frac{dc}{c} = -\frac{\dfrac{P_e}{K^*}}{E_1 - \dfrac{E_2 E_3}{E_3 + E_4}}, \tag{1}$$

where

$$E_1 = \frac{3\mu I_a}{\pi(3K + 4\mu)},$$

$$E_2 = \frac{3\mu}{2\pi(3K + 4\mu)}(3I_a - 4\pi),$$

$$E_3 = \frac{\alpha^2\left(3 - \dfrac{9I_a}{4\pi}(3K + \mu)\right)}{(1 - \alpha^2)(3K + 4\mu)} + \frac{3\mu I_a}{4\pi(3K + 4\mu)},$$

$$E_4 = \frac{\left(3 - \dfrac{9I_a}{4\pi}\right)(3K + \mu)}{(2(1 - \alpha^2)(3K + 4\mu))} - \frac{3\left(1 - \dfrac{\pi}{I_a}\right)}{2(3K + 4\mu)},$$

$$I_a = \frac{2\pi\alpha}{(1 - \alpha^2)^{3/2}}(\mathrm{Cos}^{-1}(\alpha) - \alpha\sqrt{1 - \alpha}),$$

where c is the volume fraction of the inclusion, p_e is the effective pressure, K^* is the effective bulk modulus, K and μ are the bulk modulus and shear modulus of the rock matrix, respectively, and α is the aspect ratio of the inclusion. If $dc/c \leq -1$, then the crack is

assumed to be closed. Equation (1) states that the pore volume change is a function of pore aspect ratio and effective pressure if the matrix elastic properties are known. Concentration of a certain group of cracks at pressure p_n is related to its concentration at zero effective pressure by

$$c_{nm} = c_{0m}\left(1 + \frac{dc}{c}(\alpha_{0m}, p_n)\right). \tag{2}$$

In this section and the next, subscript n means that the parameter is pressure dependent and m means that the parameter is a function of pore aspect ratio, subscript 0 refers to status of zero effective pressure. If we assume the crack (pore) is in shape of spheroid and the primary geometric change of the crack is variation of the shortest axis in response to the applied stress field, we have

$$\frac{d\alpha}{\alpha} = \frac{dc}{c}. \tag{3}$$

Thus we can relate the aspect ratio change to its original status at zero effective pressure by:

$$\alpha_{nm} = \alpha_{0m}\left(1 + \frac{d\alpha}{\alpha}(\alpha_{0m}, p_n)\right) = \alpha_{0m}\left(1 + \frac{dc}{c}(\alpha_{0m}, p_n)\right). \tag{4}$$

From Eqs. (2) and (4), the volume concentration of a certain type of crack and its aspect ratio at any pressure can be related by:

$$c_{nm} = \frac{c_{0m}}{\alpha_{0m}}\alpha_{nm}. \tag{5}$$

In summary, Eqs. (1)–(5) describe how concentration and shape of pores with a certain initial volume and aspect ratio change with applied stress. By assumption of spheroidal shape and primary deformation in direction of the shortest axis, the change of aspect ratio is equal to the fractional pore concentration change. Both changes are related to its initial status (zero effective pressure), so that we only need to know the pore aspect ratio spectrum at one stress status (e.g. the zero effective pressure condition), then the pore aspect ratio spectrum at any pressure condition can be calculated using Eqs. (1)–(5). These treatment and simplification are critical, and make it possible to invert the pore aspect ratio spectrum from the pressure dependent ultrasonic velocity measurements.

Considering higher concentration and possible effects of crack interaction, the effective elastic moduli of the solid matrix with multiple ellipsoidal inclusions are estimated by the extended Kuster–Toksöz theory,[3] which can be written in simple matrix form as:

$$\begin{aligned} \sum_{m=1}^{M} c_{nm}P_{nm} &= b_{Kn}, \\ \sum_{m=1}^{M} c_{nm}Q_{nm} &= b_{Gn}, \end{aligned} \tag{6}$$

using notation

$$b_{Kn} = \frac{K_n^* - K}{K' - K} \cdot \frac{3K_n^* - 4\mu}{3K + 4\mu},$$
$$b_{Gn} = \frac{\mu_n^* - \mu}{\mu' - \mu} \cdot \frac{6\mu_n^*(K + 2\mu) + \mu(9K + 8\mu)}{25\mu(3K + 4\mu)}, \tag{7}$$

where the elastic moduli without superscript are for the background medium, the moduli with prime ($'$) are for the inclusion, and * indicates effective modulus, and

$$P_{nm} = \frac{1}{3} T_{iijj}(\alpha_{nm}),$$
$$Q_{nm} = T_{ijij}(\alpha_{nm}) - \frac{1}{3} T_{iijj}(\alpha_{nm}), \tag{8}$$

where T_{iijj} and T_{ijij} are scalar functions of pore aspect ratio and elastic moduli of the background medium. Their expressions can be found in the Appendix of Refs. 2, 3, 17 and 18. Substituting Eq. (5) into Eq. (6), we get

$$\sum_{m=1}^{M} \alpha_{nm} P_{nm} \frac{c_{0m}}{\alpha_{0m}} = b_{Kn},$$
$$\sum_{m=1}^{M} \alpha_{nm} Q_{nm} \frac{c_{0m}}{\alpha_{0m}} = b_{Gn}. \tag{9}$$

This is a linear equation system in the form of $\mathbf{Ax} = \mathbf{b}$, where α_{0m} is given and $x_m = c_{0m}/\alpha_{0m}$ are the roots to be solved. The pore aspect ratio spectrum at any pressure can be computed from the solution using Eqs. (4) and (5).

3. Improvement on Cheng's Methodology

Cheng's primary contribution is to describe how the pore system changes with effective pressure. However, to invert the pore aspect ratio spectra, constant porosity constraint in either of following forms is applied to solve the above linear system (Eq. (9)).

$$c(\alpha_1 = 1) = \phi - \sum_{m=2}^{M} c(\alpha_m), \tag{10}$$

$$\Delta c(\alpha_1 = 1) = -\sum_{m=2}^{M} \Delta c(\alpha_m). \tag{11}$$

This is a paradox since the algorithms in last section basically describe the sequential deformation and closing of cracks of different pore aspect ratios with increasing effective pressure, that is to say, how the pore volume changes with the effective pressure. As we discussed earlier, this small portion of pore volume change can have a significant effect

on the elastic properties of the rocks and its subtle change should not be neglected. Thus, including pressure dependent porosity data is important for reliable inversion of pore aspect ratio spectra. Although the total pore volume change is usually small (around 1%), it can be reliably measured during pressure dependent velocity measurements.[4] From Eq. (5), it is straightforward that the total porosity at any pressure can be computed by

$$\phi_{tn} = \sum_{m=1}^{M} c_{nm} = \sum_{m=1}^{M} \frac{c_{0m}}{\alpha_{0m}} \alpha_{nm}. \tag{12}$$

We can combine above equation with Eq. (9) to make the inverted pore aspect ratio spectra at different pressures comply with measured porosity change data and make the inverted results more realistic. The final linear system becomes

$$\begin{bmatrix} \alpha_{11} & \alpha_{12} & \cdots & \alpha_{1M} \\ \alpha_{21} & \alpha_{22} & \cdots & \alpha_{2M} \\ \vdots & \vdots & \vdots & \vdots \\ \alpha_{N1} & \alpha_{N2} & \cdots & \alpha_{NM} \\ \alpha_{11}P_{11} & \alpha_{12}P_{12} & \cdots & \alpha_{1M}P_{1M} \\ \alpha_{11}P_{21} & \alpha_{12}P_{22} & \cdots & \alpha_{2M}P_{2M} \\ \vdots & \vdots & \vdots & \vdots \\ \alpha_{11}P_{N1} & \alpha_{12}P_{N2} & \cdots & \alpha_{1M}P_{NM} \\ \alpha_{11}Q_{11} & \alpha_{12}Q_{12} & \cdots & \alpha_{1M}Q_{1M} \\ \alpha_{11}Q_{21} & \alpha_{12}Q_{22} & \cdots & \alpha_{2M}Q_{2M} \\ \vdots & \vdots & \vdots & \vdots \\ \alpha_{11}Q_{N1} & \alpha_{12}Q_{N2} & \cdots & \alpha_{1M}Q_{NM} \end{bmatrix} \begin{bmatrix} \frac{c_{01}}{\alpha_{01}} \\ \frac{c_{02}}{\alpha_{02}} \\ \vdots \\ \frac{c_{0M}}{\alpha_{0M}} \end{bmatrix} = \begin{bmatrix} \phi_{t1} \\ \phi_{t2} \\ \vdots \\ \phi_{tN} \\ b_{K1} \\ b_{K2} \\ \vdots \\ b_{KN} \\ b_{G1} \\ b_{G2} \\ \vdots \\ b_{GN} \end{bmatrix}. \tag{13}$$

where N is the number of the pressure measurement points and M is the number of elements of the pore aspect ratio spectrum.

4. Pressure Dependent Porosity Measurement

With increasing differential pressure, the cracks and pores with different shapes will deform or even close. This process is also a process of pore volume change, which alters the elastic and viscoelastic properties of the rocks. Therefore, it is important to monitor the pore volume change during pressure dependent ultrasonic velocity measurement. Using high resolution digital pump, pore volume change measurement can be a convenient and cost-efficient by-product of the traditional ultrasonic velocity measurement.

Figure 1 shows the diagram of pressure dependent ultrasonic velocity and porosity measurement. Both the confining pressure (P_c) and the pore pressure (P_p) are controlled by the digital pumps. The confining pressure simulates the stress produced by the overburden

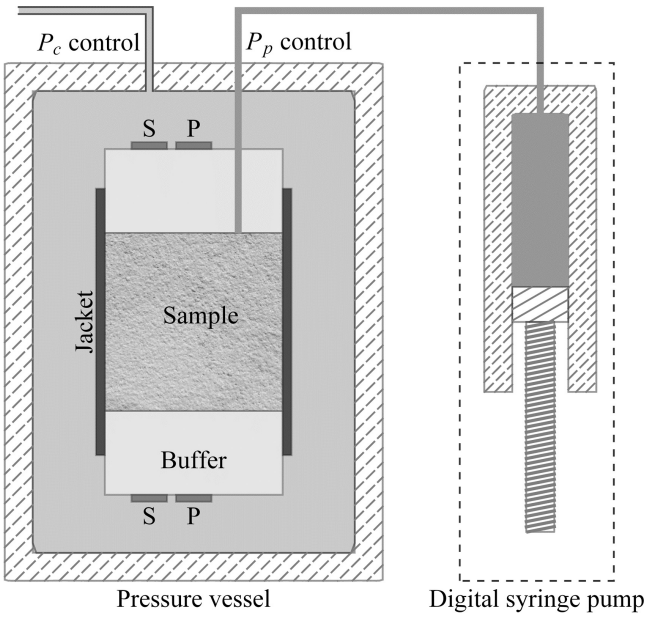

Fig. 1. Diagram of pressure dependent ultrasonic velocity and porosity measurement.

rocks. The pore fluid and the confining fluid are separated by the buffers and the jacket which holds the cylindrical core sample. During the measurement, the pore pressure is set to a desired value and then kept constant so that effect of pore fluid compressibility can be ignored. With variation of the confining pressure, the pore fluid will be absorbed into or squeezed out from the pore system, and the amount of the pore fluid volume variation can be read from the digital pump. Therefore, we can measure the velocities and pore volume changes with differential pressure (the difference between P_c and P_p) simultaneously. There is a difference between differential pressure and effective pressure, and the elastic properties of porous media are affected by the effective pressure. If the confining pressure is much higher than the pore pressure, which is our case, the difference between effective pressure and differential pressure is usually not important.

To estimate the pressure dependent porosity, we still need the traditional porosity measurement, which is often conducted at zero effective pressure using helium porosimeter. The primary uncertainty in monitoring pore volume change comes from the coupling between the core sample, the buffers and the jacket. An expedient handling is to assume that the porosity measured by the helium porosimeter equals to the porosity when the sample is properly coupled with its surroundings (buffers and jacket), usually under differential pressure around 3 MPa. With decreasing confining pressure, the pore volume increases and more fluids will be absorbed into the pore system from the reservoir tank of the digital pump. For a typical 1–1/2 inch reservoir core sample, the total pore volume change for differential pressure variation range of 3–50 MPa is around 0.1–0.5 ml. The volume of the reservoir tank of the digital pump is monitored and displayed in real time, with resolution that can be as high as 2.5 nanoliters depending on the digital pump model. At each pressure

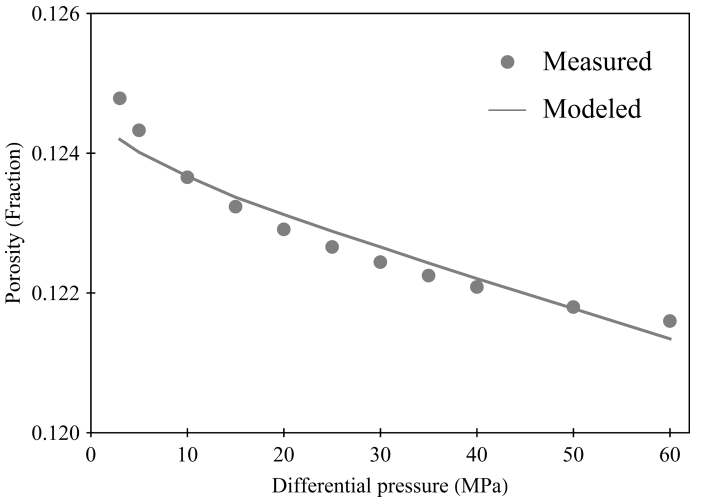

Fig. 2. Pressure dependent porosity measurement and modeling on a carbonate sample.

measurement point, we wait around 30 min for the pore fluid system to reach pressure equilibrium. This way, the measured pressure dependent porosity can be reasonably reliable. Figure 2 shows the pressure dependent porosity measurement data for a calcarenite (carbonate sands) core sample. The porosity measured by helium porosimeter is 12.5%. The total pore volume change for the core sample in this study is about 0.15 ml in the pressure range of measurement.

5. Example of Pore Aspect Ratio Spectra Inversion

For this carbonate core sample, we have also measured pressure dependent P-wave velocity and S-wave velocity under 100% water saturation, as shown in Fig. 3. With these three sets of data (pressure dependent P-wave velocity, S-wave velocity and porosity), using the improved pore aspect ratio inversion methodology, we can invert the pore aspect ratio at zero effective pressure condition. Here the number and values of the pore aspect ratios (α_{0m}) are arbitrarily given. α_{0m} describes how the complex pore structure is discretized. More elements are better for accurate representing the complex pore structure, but they can be resolved with more uncertainty. We solve Eq. (13) as an over-determined linear system in least-square sense and the total number of elements is limited by the data points. In this study, we select the initial total elements M to be 22, which is 2/3 of the data points. Another important consideration in choosing α_{0m} is that the pore aspect ratio spectrum is more densely sampled for the softer pores than for the stiffer pores because the former is more sensitive to stress change. The other input parameters are the solid rock frame bulk modulus ($K = 77\,\text{GPa}$) and shear modulus ($\mu = 36\,\text{GPa}$).

After c_{0m} is solved from Eq. (13), we know the pore aspect ratio spectrum at zero effective pressure. Then using Eqs. (4) and (5), the pore aspect ratio spectrum at any differential pressure can be computed. Figure 3 shows the pore aspect ratio spectra at differential

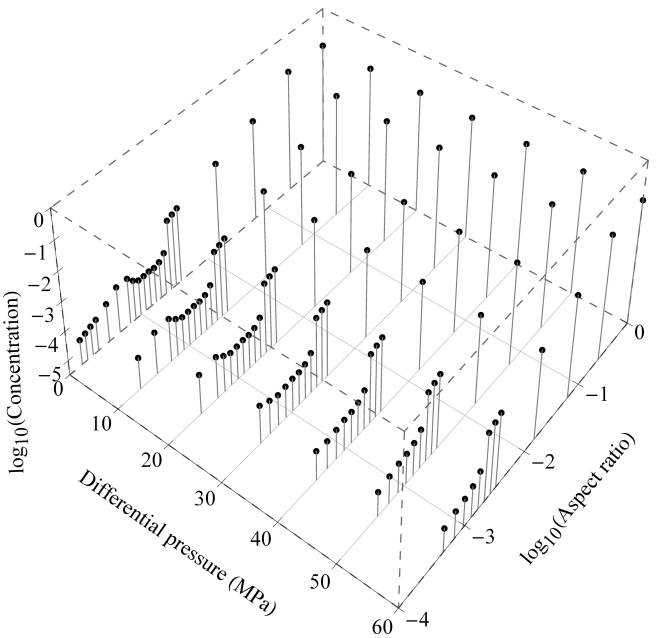

Fig. 3. Inverted pore aspect ratio spectra at different differential pressures.

pressures of 0, 10, 20, 30, 40, 50 and 60 MPa. As we can see from Fig. 3, with increasing of differential pressure, the number of elements of the pore aspect ratio spectrum decreases as the softer pores (cracks) are sequentially closed. The decrease of concentration of pores of a certain pore aspect ratio is more observable for the softer pores than the stiffer pores.

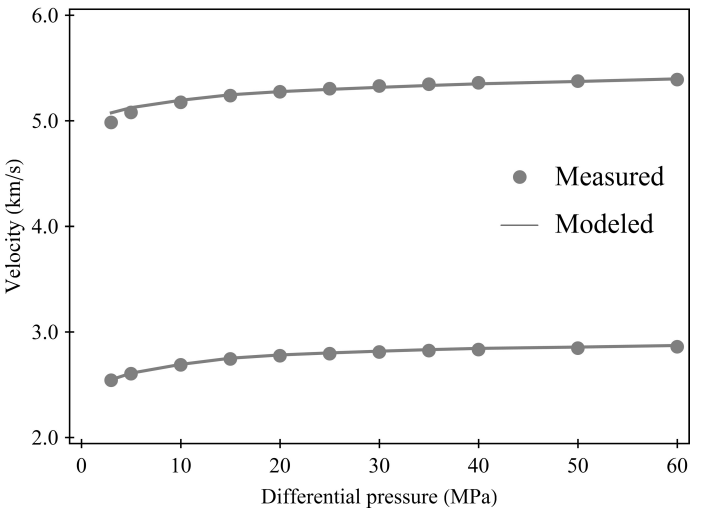

Fig. 4. Comparison between measured and modeled ultrasonic velocities (100% water saturation) on a carbonate sample. The upper data points are for the P-wave velocity and the lower data points are for the S-wave velocity.

The uneven distribution in the dense section of the pore aspect ratios at zero differential pressure means the inverted concentrations for pores of certain pore aspect ratios are zero.

The inversion process is also a modeling process. Using the inverted pore aspect ratio spectra and Eq. (12), we can model the pressure dependent porosity changes. As shown in Fig. 2, the modeled porosity changes generally fit well with the measured porosity data. Using Kuster–Toksöz theory, the modeled P-wave velocity and S-wave velocity are shown in Fig. 4. The modeled velocities fit well with the measured data. Since the inverted pore aspect ratio spectra fit well with the measured porosity changes, it is logical to believe that the inverted pore aspect ratio spectra using our improved methodology are more realistic than those inverted by Cheng's[3] methodology because closing and deformation of pores with various pore aspect ratios have no effect on the total porosity in the latter case.

6. Application of Inverted Pore Aspect Ratio Spectra

Originally, the concept of pore aspect ratio spectrum was brought up to describe the complex pore structure and its relation with the effective elastic properties of the porous medium.[3] From variation of the pore aspect ratio spectrum, we can predict the stress effect on the elastic properties, especially the seismic wave velocities of the rocks. In seismic exploration, as seismic waves pass through the subsurface rock formations, it will produce stress disturbance. This stress disturbance will cause dynamic deformation of the porous rock. The pores with different pore aspect ratio will deform differently. The pore fluid in softer pores with smaller pore aspect ratio will be squeezed harder and produce higher pressure disturbance than the pore fluid in the stiffer pores. The pore fluids exchange between pores of different pore aspect ratios is chaotic and not in step with seismic wave propagation. This mechanism is called squirt flow and can cause significant attenuation of the seismic waves. If we know the pore structure (the pore aspect ratio spectrum), theoretically we should be able to quantify attenuation of the seismic waves caused by fluid exchange between pores of different shapes. This may be a more important and practical application of pore aspect ratio spectrum.

Within the framework of the Biot theory, Tang[8] brought up a unified model to describe wave propagation in porous media affected by the Biot flow and the squirt flow. Similar to the BISQ (Biot-squirt) model,[5,19] the high frequency limit of Tang's model is equivalent to that of the Biot theory, and the lower limit of Tang's model is below the lower limit of the Biot–Gassman theory and close to the drained lower limit predicted by the BISQ model. So Tang's model is for drained condition and is not applicable to the general subsurface scenarios in seismic exploration.[20]

For rocks under subsurface conditions, if we assume the wavelength is much larger than the grain size, compared to the Biot flow, the communication of pore fluids between cracks and stiff pores is more eligible to be treated as local flow in closed boundary. As long as the pore fluids are not completely relaxed, the effective bulk modulus should always be higher than that predicted by the Biot–Gassmann theory. At high frequency limit, the pore fluids in the cracks are locked and the cracks are effectively stiff, so the velocity is higher than the

high limit predicted by the Biot–Gassmann theory; at low frequency limit, the pore fluids in the cracks are completely relaxed (reaches pressure balance with the pore fluid in the stiff pores), the cracks are effectively soft, then the velocity should be equal to that predicted by the Gassmann equation (lower limit of the Biot theory). Under this principle, following Tang's procedure, we have re-derived and modified Tang's model as:

$$K^* = K_d + \frac{n^2}{\dfrac{n-\phi}{K_m} + \dfrac{\phi}{K_f} - \Delta S(\omega)}, \tag{14}$$

where K^* is the effective bulk modulus without considering effect of the Biot flow, K_d is the dry bulk modulus and n is the Biot coefficient. The detailed derivation can be found in Yao's[20] dissertation. $\Delta S(\omega)$ is the term related to squirt flow and instantaneous storage capacity of the cracks, and it is represented by:

$$\Delta S(\omega) = S_{\max} - S(\omega), \tag{15}$$

where

$$S_{\max} = \frac{8\pi\varepsilon K_d(\nu_m - 1)(K^* - K_m)}{3\mu(K^* - K_d)K_d},$$

$$S(\omega) = \frac{\dfrac{8}{3}\pi\varepsilon\dfrac{1-\nu_m}{\mu_m}f(\zeta)\left(\dfrac{1/K_d - 1/K_m}{1/K_d - 1/K^*} - f(\zeta)\right)}{1 + \dfrac{4(1-\nu_m)K_f}{3\alpha\mu_m}(1 - f(\zeta))},$$

with

$$f(\zeta) = \frac{2J_1(\zeta)}{\zeta J_0(\zeta)},$$

$$\zeta = \sqrt{\frac{3i\omega\eta}{\alpha^2 K_f}},$$

where ω is the angular frequency, η is the pore fluid viscosity, α is the pore aspect ratio, ν_m is the Poisson's ratio of the background medium and ε is the crack density, which can be calculated by

$$\varepsilon = \frac{\phi_c}{2\pi\alpha}, \tag{16}$$

where ϕ_c is the concentration of cracks with pore aspect ratio α. $S_{\max}$ is the term related to maximum fluid volume transferred from cracks to stiff pores if the cracks are completely relaxed ($\omega \to 0$). Similar to the treatment of DEM model,[21,22] for multiple inclusions of cracks with different aspect ratios, the effect of cracks can be added differentially to the system and the effective modulus (K^*) is updated iteratively. Since the squirt flow is a nonlinear process, the differential scheme is more rational because it considers the pore pressure increase in the stiff pores while the pore fluid in the soft pores is squeezed into

the stiff pores. The original Tang's model[8] assumes the pore pressure in the stiff pores does not increase while the pore fluid in soft pores is squeezed into the stiff pores. Therefore, the original Tang model[8] might break down even at moderate low crack density because of overestimation of the squirt flow. The modified Tang's model using differential scheme does not break at high crack density. The final computed effective modulus (K^*) is substituted into the Biot theory formulated by Tang and Cheng[23] to calculate the wave velocities under influence of Biot flow and squirt flow. The velocity dispersion and attenuation can be calculated by,[8]

$$\nu = \frac{\omega}{\mathrm{Re}[k]}, \tag{17}$$

$$Q^{-1} = \frac{2\mathrm{Im}[k]}{\mathrm{Re}[k]}, \tag{18}$$

where Q is the quality factor and k is the wavenumber. $\mathrm{Re}[k]$ and $\mathrm{Im}[k]$ are the real part and imaginary part of k, respectively.

For the carbonate rock sample under study, we have shown that the pore volume change due to closure and deformation of the crack pores generally agrees with the measured porosity change, and the pressure dependent velocity data can be modeled with good match using Kuster–Toksöz[17] model, thus we have reasonable confidence in the inverted pore aspect ratio spectra. We have also measured the dry rock P-wave and S-wave velocities, as shown in Fig. 5. The inverted pore aspect ratio spectra are then put into the modified Tang's model to predict the velocity dispersion and attenuation. The other input parameters for

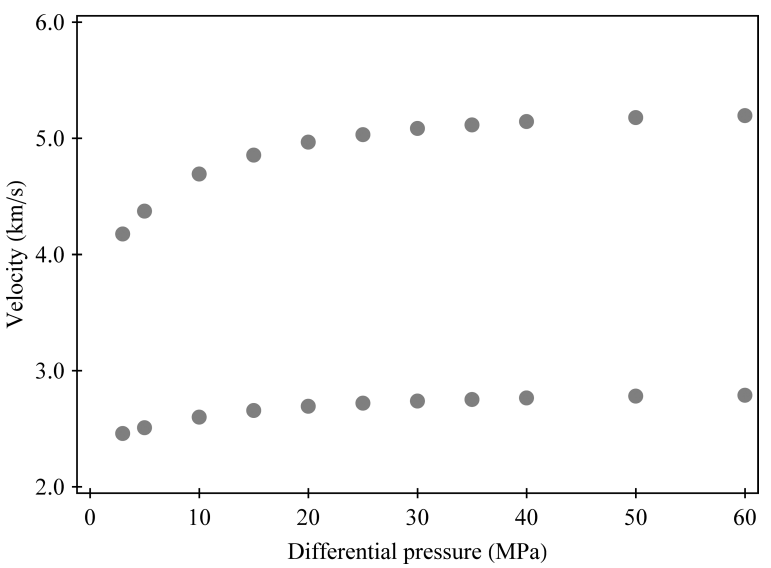

Fig. 5. Measured P-wave velocity (the upper data points) and S-wave velocity on the dry carbonate rock sample.

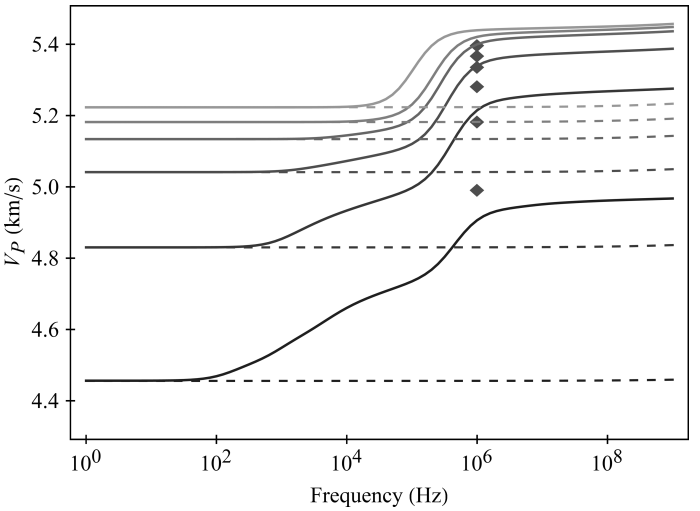

Fig. 6. Prediction of fast P-wave velocity dispersion at different differential pressures. Solid curves are predicted by modified Tang's model, dashed lines are velocity dispersion predicted by the Biot theory. Darker curve represents lower differential pressure. Data points at 10^6 Hz are measured ultrasonic P-wave velocities at different differential pressures and full water saturation.

prediction of velocity dispersion and attenuation are rock permeability of 1 mD, pore fluid viscosity of 1 cp and tortuosity of 2.4.

Figure 6 shows prediction of the fast P-wave velocity dispersion at different differential pressures. For clarity, we only show predictions for alternating pressure measurement points (3, 10, 20, 30, 40, 60 MPa). The solid curves are predicted by the modified Tang's model, and the dashed lines are velocity dispersion predicted by the Biot theory. Data points at 10^6 Hz are measured ultrasonic P-wave velocities at corresponding differential pressures and

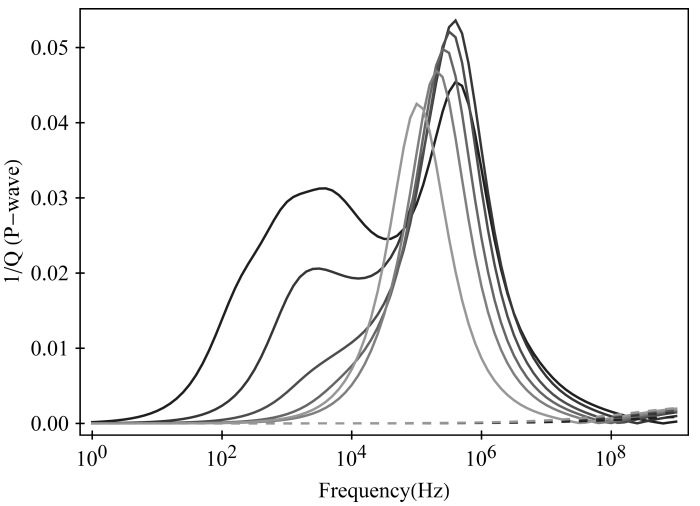

Fig. 7. Fast P-wave attenuation at different differential pressures corresponding to Fig. 6.

in 100% water saturation. It can be seen that the predictions match fairly well with the measured ultrasonic P-wave velocities. For this sample, the P-wave dispersion are primarily caused by squirt flow. The amount of dispersion caused by the Biot flow is small and occurs at very high frequency (around 10^9 Hz). The P-wave dispersion is stronger at the lower differential pressures when most of the soft pores are open. With increasing differential pressure, soft pores are being sequentially closed and the dispersion caused by squirt flow decreases. The characteristics of P-wave velocity dispersion at low differential pressure comply with the laboratory observation.[14] The corresponding fast P-wave attenuation is shown in Fig. 7. The attenuation induced by squirt flow is dominant and can occur at a wide frequency range, while attenuation caused by the Biot flow is negligible and occurs at much higher frequency. With increasing differential pressure, the attenuation frequency band generally becomes narrower.

7. Conclusions

Based on Cheng's pore aspect ratio spectrum inversion methodology, we have related closure and deformation of the soft pores to the measured pressure dependent porosity data. With this additional constraint, the inverted pore aspect ratio spectra are more realistic. Combining the improved pore aspect ratio spectrum inversion methodology and the adapted Tang's model, we established a general framework for prediction of seismic wave attenuation and dispersion using pressure dependent ultrasonic velocity and pore volume change measurement data.

Acknowledgments

We thank Fluid/DHI consortium sponsors for supporting the consortium and this study. We thank Allen Li for his careful edition to improve the readability of the manuscript.

References

1. A. Nur, Effects of stress and fluid inclusions on wave propagation in rocks, PhD thesis, Massachusetts Institute of Technology (1969).
2. M. N. Toksöz, C. H. Cheng and A. Timur, Velocities of seismic waves in porous rocks, *Geophysics* **41** (1976) 621–645.
3. C. H. Cheng, Seismic velocities in porous rocks — Direct and inverse problems, PhD thesis, Massachusetts Institute of Technology (1978).
4. D.-H. Han, Effects of porosity and clay content on acoustic properties of sandstones and consolidated sediments, PhD thesis, Stanford University (1986).
5. J. Dvorkin, G. Mavko and A. Nur, Quirt flow in fully saturated rocks, *Geophysics* **60** (1995) 97–107.
6. M. Chapman, S. V. Zatsepin and S. Crampin, Derivation of a microstructural poroelastic model, *Geophys. J. Int.* **151** (2002) 427–451.
7. C. Wei and K. K. Muraleetharan, Acoustical characterization of fluid-saturation porous media with local heterogeneities: Theory and application, *Int. J. Solids Struct.* **43** (2006) 982–1008.

8. X. M. Tang, A unified theory for elastic wave propagation through porous media containing cracks — An extension of Biot's poroelastic wave theory, *Sci. China Earth Sci.* **54** (2011) 1141–1152.
9. X. M. Tang, X.-L. Chen and X.-K. Xu, A cracked porous medium elastic wave theory and its application in interpreting acoustic data from tight formations, *Geophysics* **77**(6) (2012) D245–D252.
10. S. R. Pride and J. G. Berryman, Linear dynamics of double-porosity dual-permeability materials: I. Governing equations and acoustic attenuation, *Phys. Rev. E* **68** (2003).
11. S. R. Pride and J. G. Berryman, Linear dynamics of double-porosity dual-permeability materials: II. Fluid transport equations, *Phys. Rev. E* **68** (2003).
12. J. G. Berryman, Effective medium theories for multicomponent poroelastic composites, *J. Eng. Mech.* **132** (2006) 519–531.
13. J. W. Spencer, Stress relaxations at low frequencies in fluid saturated rocks: Attenuation and modulus dispersion, *J. Geophys. Res.* **86** (1981) 1803–1812.
14. M. L. Batzle, D.-H. Han and R. Hofmann, Fluid mobility and frequency-dependent seismic velocity — Direct measurements, *Geophysics* **71** (2006) N1–N9.
15. F. Yan, D.-H. Han and Q. Yao, Effective porosity for Gassmann fluid substitution, *SEG Extended Abstracts* **83** (2013) 2861–2865.
16. J. D. Eshelby, The determination of the elastic field of an ellipsoidal inclusion, the related problems, *Proc. Roy. Soc. London, Ser. A* **241** (1957) 376–396.
17. G. T. Kuster and M. N. Toksöz, Velocity and attenuation of seismic waves in two phase media, *Geophysics* **39** (1974) 587–618.
18. C. H. Cheng and M. N. Toksöz, Inversion of seismic velocities for the pore aspect ratio spectrum of a rock, *J. Geophys. Res.* **84** (1979) 7533–7543.
19. J. Dvorkin and A. Nur, Dynamic poroelasticity: A unified model with the squirt and the Biot mechanisms, *Geophysics* **58** (1993) 524–533.
20. Q. Yao, Velocity dispersion and wave attenuation in reservoir rocks: PhD thesis, University of Houston (2013).
21. M. P. Cleary, I. W. Chen and S. M. Lee, Self-consistent techniques for heterogeneous media, *Am. Soc. Civil Eng. J. Eng. Mech.* **106** (1980) 861–887.
22. A. N. Norris, A differential scheme for the effective moduli of composites, *Mech. Mater.* **4** (1985) 1–16.
23. X. M. Tang and C. H. A. Cheng, *Quantitative Borehole Acoustic Methods* (Elsevier, 2004).